Journal of
*Marine Science
and Engineering*

Article

Numerical Investigation of Hydrodynamic Characteristics of a Rim-Driven Thruster Coupled with an Underwater Vehicle

Bao Liu [1,2,3,4], Wu Ouyang [1,2,3,4], Xinping Yan [1,2,3,4] and Maarten Vanierschot [5,6,*]

[1] State Key Laboratory of Maritime Technology and Safety, Wuhan University of Technology, Wuhan 430063, China; baoliu@whut.edu.cn (B.L.); ouyangw@whut.edu.cn (W.O.); xpyan@whut.edu.cn (X.Y.)
[2] East Lake Laboratory, Wuhan 420202, China
[3] School of Transportation and Logistics Engineering, Wuhan University of Technology, Wuhan 430063, China
[4] Reliability Engineering Institute, National Engineering Research Center for Water Transport Safety, Wuhan 430063, China
[5] Department of Mechanical Engineering, KU Leuven, B-3001 Heverlee, Belgium
[6] Material Science, Innovation and Modelling (MaSIM) Research Focus Area, North-West University, Mmabatho 2745, South Africa
[*] Correspondence: maarten.vanierschot@kuleuven.be

Abstract: In this paper, the hydrodynamic characteristics of a rim-driven thruster (RDT) behind the hull of an underwater vehicle are investigated. The studied underwater vehicle is the benchmark DARPA (Defense Advanced Research Projects Agency) suboff model, with and without full appendages. In order to verify and validate the numerical model, a grid sensitivity analysis is made for the AFF-1, AFF-8 and the ducted propeller cases, respectively. Then, the resistance and pressure distribution over the surface of the suboff with and without appendages are compared with available experimental measurements and good correlations were observed. As for the propeller, a well-studied ducted propeller, the 19A duct in combination with Ka-47 blades, is employed, and the numerical results exhibit a close relationship with the available experimental data under a wide range of advance coefficients. Afterwards, the self-propulsion characteristics of the suboff models propelled by RDTs using different duct configurations are studied, more specifically, the unsteady effects of the flow field induced by the interactions between propeller and hull under various working conditions. The results indicate that due to the influence of the hull, the RDTs operate in different working conditions compared to open water and exhibit distinct hydrodynamic characteristics. Moreover, the duct profile can have a significant effect on the unsteady pressure fluctuations in the flow field, especially in the vicinity of the propeller.

Keywords: hydrodynamic characteristics; rim-driven thruster; self-propulsion; unsteady effects

Citation: Liu, B.; Ouyang, W.; Yan, X.; Vanierschot, M. Numerical Investigation of Hydrodynamic Characteristics of a Rim-Driven Thruster Coupled with an Underwater Vehicle. *J. Mar. Sci. Eng.* **2024**, *12*, 1838. https://doi.org/10.3390/jmse12101838

Academic Editor: Stefano Gaggero

Received: 10 September 2024
Revised: 2 October 2024
Accepted: 11 October 2024
Published: 14 October 2024

1. Introduction

It is known that for underwater vehicles, noise reduction is of crucial importance as it is directly related to the capability of invisibility. However, in conventional designs, the propeller is driven by a central shaft that protrudes from the hull and is inclined, which causes significant mechanical vibrations and noise, resulting in energy losses as well [1]. In recent years, the innovative rim-driven thruster (RDT) has become a popular research topic and has the potential to overcome the above issues. RDTs have a much more compact design by integrating the propeller with the driving motor. The elimination of a transmission shaft can therefore substantially improve the noise performance of the thruster, indicating that the RDT is more suitable for underwater vehicles.

Even though the RDT has exhibited some outstanding advantages over conventional propellers, such as a flexible installation, high power density and a more efficient space utilization [2], some critical problems still remain to be solved regarding the structural design and hydrodynamic performance evaluation. In order to explore the potential of

RDTs, a significant amount of research has been conducted. For example, there are some studies focusing on motor design and its control system [3–6]. These studies attempted to find a motor design that is applicable to RDTs with a higher efficiency and power density. Different motor designs have been proposed and analyzed, such as an induction motor, high-temperature superconducting motor, switched reluctance motor, etc. Even though some kinds of motors showed superior performance, they often required a demanding cost to build and can hardly be employed for general applications. Among them, the permanent magnet motors are currently the most adopted ones due to their simple structure and easy access.

In terms of hydrodynamic analysis, current studies on RDTs mainly focus on numerical modeling and general hydrodynamic performance prediction of the propeller. For instance, Dubas et al. [7] investigated the rotor-stator interaction with the steady frozen rotor method and the unsteady sliding mesh approach. In order to improve the prediction accuracy, Liu et al. [8,9] adopted transition turbulence models to better capture the laminar-to-turbulent transition in the boundary layer of the propeller, and it was shown that the transition models demonstrated enhanced performance prediction in propeller torque. Similar findings were also observed in the work of Grlj et al. [10] for open water propellers. As the RDT contains both rotating and stationary parts, the influence of computational domain division on the performance prediction of the propeller was studied by Li et al. [11], and they concluded that the gap flow and wake structure were affected by the computational domain decomposition. Due to the similarities in structural design, Liu and Vanierschot [12] investigated the hydrodynamic performance of a rim-driven thruster and a ducted propeller with the same configurations. Song et al. [13] made a comparison study between two types of RDTs, i.e., the hub-type and hubless-type using CFD simulations. It was found that compared to the hub RDT, the hubless RDT showed a higher hydrodynamic efficiency without the resistance caused by the central hub. Liu et al. [14] investigated the influence of scale effects on the open water performance of an RDT employing transition models. Afterwards, the influence of bearings on the open water performance of RDTs was explored in Liu et al. [15], considering two representative bearing types. Their results indicated that the presence of the bearings in the gap has an influence on the overall performance of the thruster by changing the flow regime in the gap and the interactions between different components of the RDT. The wake dynamics of RDTs have also been studied by Liu et al. [16] and Gaggero [17] in order to better understand the evolution of vortical structures behind the propeller and their impacts on the RDT noise performance. Moreover, the concept of rim-driven technology is also applied to other fields, such as tidal turbines [18].

Several studies have been carried out on the optimization design of RDTs. Gaggero [19] proposed a simulation-based optimization framework for the design of RDT propellers. A multi-objective algorithm was employed to take into account the efficiency and cavitation performance. The results indicated that after optimization, the cavitation performance of the propeller, regardless of the number of blades, was improved significantly. Zhai et al. [20] employed a parametric method to define the duct profile and finally a gain of 3.3% in efficiency was realized. In the work of Liu et al. [21], the adjoint approach was utilized to optimize the profile of an RDT duct. Compared to the baseline symmetric duct profile, the optimized duct achieved a higher efficiency as well as a reduced cavitation risk. A multi-parameter collaborative optimization framework was proposed by Nie et al. [22] to improve the efficiency of RDTs based on the response surface method.

From the above summary, it can be seen that currently, most studies on RDTs are based on the assumption that the RDT operates in open water conditions without the influence of other objects, such as a vessel hull. However, it is of paramount importance to take into account the propeller–hull interactions when fully evaluating the performance of a propeller, as the flow behavior is totally different from open water conditions [23–25]. Therefore, some researchers have set out to quantify the effects of propeller–hull interactions for conventional propulsion systems in order to find better solutions for optimal design [26,27]. The present work is therefore intended to investigate the effects of the hull of an underwater vehicle on the hydrodynamic characteristics of a rim-driven thruster. The benchmark DARPA (Defense Advanced Research Projects Agency) suboff model is employed for this study, as there is a large amount of experimental data available, which can be used to validate the numerical model. The remainder of the paper follows the structure in the following way: the model set-up and its validation study are described in Section 2, including the comparison of resistance against experimental data for the suboff model with and without appendages and the open water performance of the ducted propeller. The analysis of hydrodynamic performance of the RDT with and without the influence of a hull is presented in Section 3. Finally, some conclusions are drawn based on the results in Section 4.

2. Model Set-Up and Validation Study

2.1. Numerical Model

In the present work, Computational Fluid Dynamics (CFD) simulations using the RANS and URANS approaches are employed to resolve the flow around the submarine and the propeller. The governing equations for the flow are given as

$$\frac{\partial u_i}{\partial x_i} = 0, \tag{1}$$

$$\rho\left(\frac{\partial u_i}{\partial t} + u_j\frac{\partial u_i}{\partial x_j}\right) = -\frac{\partial p}{\partial x_i} + \frac{\partial}{\partial x_j}\left[\mu\left(\frac{\partial u_i}{\partial x_j} + \frac{\partial u_j}{\partial x_i}\right)\right] + \frac{\partial}{\partial x_j}\left(-\rho\overline{u_i' u_j'}\right), \tag{2}$$

where ρ is the fluid density, $u_i\ (i,j = 1,2,3)$ are the ensemble averaged velocity components, t is the flow time, p is the pressure, μ is the dynamic viscosity, and $-\rho\overline{u_i' u_j'}$ is the Reynolds stress term. For incompressible Newtonian flows, the Reynolds stresses can be related to the mean strain rate and eddy viscosity as follows,

$$-\rho\overline{u_i' u_j'} = \mu_t\left(\frac{\partial u_i}{\partial x_j} + \frac{\partial u_j}{\partial x_i}\right) - \frac{2}{3}\rho k\delta_{ij}, \tag{3}$$

where μ_t is the turbulent viscosity and δ_{ij} is the Kronecker symbol. The SST (Shear Stress Transport) $k-\omega$ turbulence model developed by Menter [28] is chosen as turbulence closure.

The steady and implicit unsteady solvers in Star-CCM+ are employed for the calculations. The all y^+ wall treatment is adopted and no transitional modeling is involved. The SIMPLE (Semi-Implicit Method for Pressure Linked Equation) segregated algorithm is adopted to link velocity and pressure. In this study, the moving reference frame approach is utilized for the steady simulations and the sliding mesh technique for the unsteady ones. Some important parameters are monitored to ensure that the calculations are fully converged. For the unsteady simulations, the time step size is equal to 1 degree of propeller rotation with an inner iteration number of 8.

2.2. DARPA Suboff Models

The hull of the underwater vehicle in this study is the benchmark DARPA (Defense Advanced Research Projects Agency) suboff without and with full appendages, also referred as suboff AFF-1 and AFF-8, respectively, as shown in Figure 1. These models were selected because public experimental data are available for validation, including hull resistance and flow field details. The basic parameters of the submarine are provided in Table 1, and the geometric details can be found in Huang and Liu [29].

Table 1. Main parameters of the DARPA suboff model.

Parameter	Symbol	Unit	Value
Reynolds number	Re_S	-	1.2×10^7
Hull Diameter	D_S	m	0.508
Hull Length	L	m	4.356

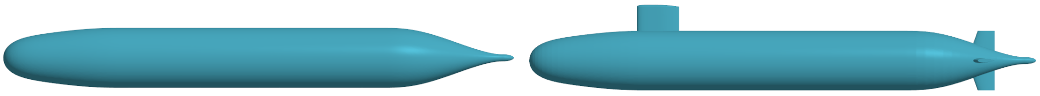

(**a**) AFF-1.

(**b**) AFF-8.

Figure 1. A general view of the DARPA suboff models: (**a**) AFF-1 without and (**b**) AFF-8 with full appendages, respectively.

2.2.1. Mesh Generation and Validation

For all simulations in the present study, the computational domains share a similar topology. For example, the computational domain for the simulations of the DARPA suboff submarines with and without appendages has a cylindrical shape, in which the inlet is located 1L ahead of the bow of the submarine, and the outlet is placed 2L away from the stern of the submarine. The radius of the cylinder is $5D_s$, where D_s is the diameter of the submarine. The boundary conditions are defined as follows: a velocity inlet with uniform incoming flow is set at the inlet, a pressure outlet with constant ambient pressure is set at the outlet, a slip wall is set for the side surface of the domain and no-slip walls are set for the solid surfaces of the submarine, as summarized in Table 2.

Table 2. Boundary condition definition.

Boundary	Velocity	Pressure
Inlet	Calculated by J	$\frac{\partial p}{\partial n} = 0$
Outlet	$\frac{\partial v}{\partial n} = 0$	Constant
Suboff surfaces	v=0	$\frac{\partial p}{\partial n} = 0$
Domain side surface	$\frac{\partial v}{\partial n} = 0$	$\frac{\partial p}{\partial n} = 0$

The mesh generation is performed within Star-CCM+, in which unstructured trimmed grids are used to discretize the computational domain. Some local refinements are added to locations with high curvature or appendages in order to better capture the flow details. The surface and volume meshes for the DARPA suboff models are presented in Figures 2 and 3. The all y^+ wall function is employed, which resolves the boundary layer with varied near-wall treatment based on local y^+,

$$y^+ = y\rho u_\tau/\mu, \tag{4}$$

in which y is the distance normal to the wall, $u_\tau = \sqrt{\tau_w/\rho}$ is the friction velocity and τ_w is the wall shear stress.

Afterwards, the grid assessment procedure proposed by Roache [30] is adopted to estimate the grid discretization error. As suggested by the procedure, three sets of meshes have been generated in order to reduce the numerical uncertainty. As all the meshes are unstructured in the present study, the refinement ratio between meshes is calculated based on the total number of grid cells in the entire computational domain, notably,

$$r_{21} = \left(\frac{N_2}{N_1}\right)^{1/d} > 1 \tag{5}$$

in which N_1 and N_2 is the number of grid cells for the coarse and medium mesh, respectively, and d is the dimension of the problem, which is 3 in this case. For the refinement ratio between medium and fine meshes, the same procedure can be applied. Moreover, the Grid Convergence Index (*GCI*) is introduced to quantify the grid uncertainty.

$$e_{21} = |\frac{\phi_1 - \phi_2}{\phi_1}|, \tag{6}$$

$$GCI_{21} = \frac{1.25e_{21}}{r_{21}^{p} - 1}, \tag{7}$$

where e_{21} is the relative error between two meshes, ϕ_1 and ϕ_2 are the results from different meshes, 1.25 is the safety factor when three or more meshes are employed, r_{21} is the refinement ratio as defined in Equation (5) and p is the order of numerical accuracy, which is 2 in this study.

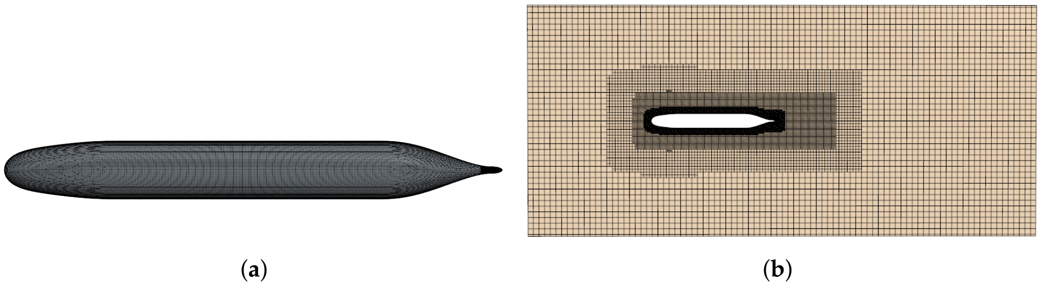
(a) (b)

Figure 2. Mesh discretization for the suboff AFF-1 model. (**a**) Surface mesh. (**b**) Volume mesh.

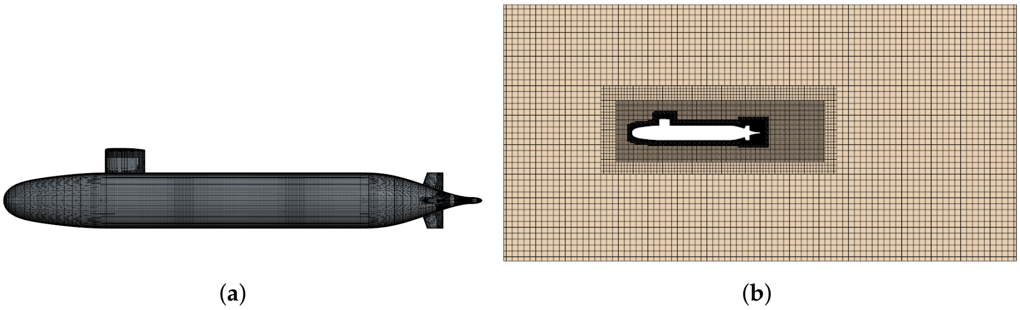
(a) (b)

Figure 3. Mesh discretization for the suboff AFF-8 model. (**a**) Surface mesh. (**b**) Volume mesh.

The results of the mesh sensitivity analysis for the DARPA suboff models with and without appendages are presented in Tables 3 and 4, respectively. For the suboff AFF-1 model, it can be seen that the predicted resistance by the different meshes is very close. The convergence is non-monotonic, yet the *GCI* value decreases a little. As for the AFF-8 model, non-monotonic convergence is also observed. The *GCI* values are slightly higher, yet they are still within acceptable ranges. Moreover, the experimental measurements by Liu and Huang [31] are also provided for comparison and reasonable agreement is noted in both cases.

Table 3. Discretization error estimation for suboff model: AFF-1.

Mesh Density	Total Cells	Refinement Ratio	Resistance	*GCI*
Coarse	676,834	-	86.72 N	-
Medium	1,316,427	1.25	85.88 N	1.7%
Fine	2,533,748	1.24	86.61 N	1.6%
Experiment			87.4 N	

Table 4. Discretization error estimation for suboff model: AFF-8.

Mesh Density	Total Cells	Refinement Ratio	Resistance	*GCI*
Coarse	1,301,011	-	102.67 N	-
Medium	2,113,258	1.17	102.77 N	0.26%
Fine	3,185,314	1.15	101.49 N	3.9%
Experiment			102.3 N	

2.2.2. Comparison with Experimental Measurements

To further substantiate the fidelity of the numerical model, the pressure and skin friction coefficients on the AFF-1 and AFF-8 surfaces along the longitudinal direction are provided in Figures 4 and 5. Apparently, the pressure and skin friction distributions predicted by CFD match the experimental results very well. In the case of the AFF-8, the sudden changes in pressure distribution at the location of the sail and rudder fins are caused by the presence of these appendages. Furthermore, the velocity field in the wake of the AFF-8 model is also compared between CFD and Experimental Fluid Dynamics (EFD), as shown in Figures 5b,c. It needs to be noted that the displayed velocity is the streamwise velocity, which has been non-dimensionalized by the free-stream velocity. It can be observed that the pattern of the velocity distribution is quite similar, and a V-shaped carving is clearly detected downstream of the sail, which is caused by the depletion of the boundary layer at the center [32].

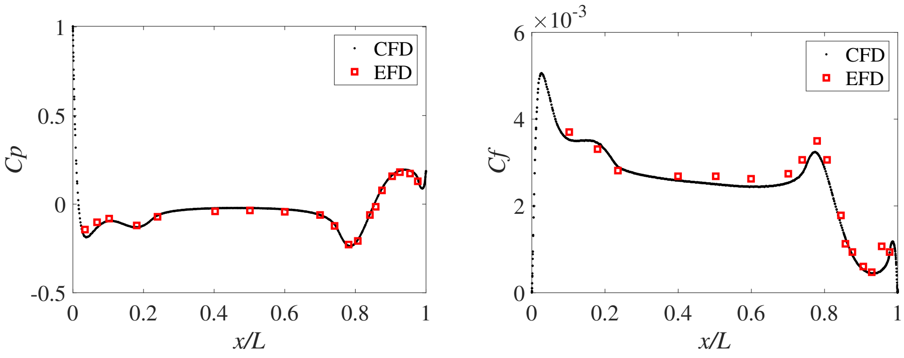

(**a**) (**b**)

Figure 4. Comparison of non-dimensional parameters between CFD and EFD for the AFF-1 model. (**a**) Pressure coefficient C_p distribution. (**b**) Skin friction coefficient C_f distribution.

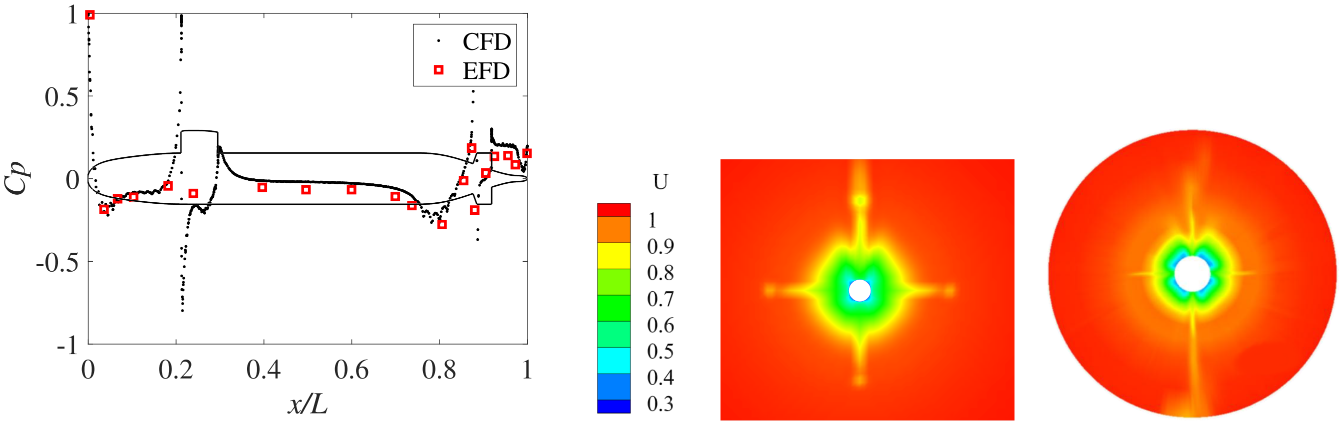

(**a**) (**b**) (**c**)

Figure 5. Comparison of non-dimensional parameters between CFD and EFD for the AFF-8 model. (**a**) Pressure coefficient C_p distribution. (**b**) Velocity distribution at the propeller plane ($x/L = 0.978$): CFD. (**c**) Velocity distribution at the propeller plane ($x/L = 0.978$): EFD.

2.3. Ducted Propeller and Rim-Driven Thruster

Due to a lack of experimental data for the rim-driven thruster, a ducted propeller is used instead to validate the numerical model for the propeller simulations as it is very similar to an RDT in structural design. The well-studied ducted propeller with Ka4-70 blades inside a MARIN 19A duct is selected, and the physical model is provided in Figure 6. Detailed geometric information about the ducted propeller can be found in Oosterveld [33], as well as experimental data for open water tests.

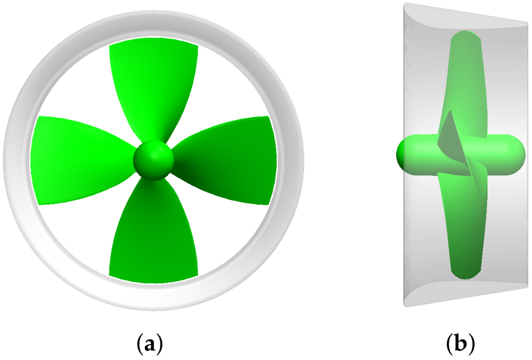
(**a**) (**b**)

Figure 6. Physical model of the ducted propeller. (**a**) Front view. (**b**) Side view.

2.3.1. Mesh Generation and Validation

The set-up of the computational domain follows the previous study of Liu et al. [8,21], in which a cylinder was adopted. The boundary conditions are summarized in Table 5. The inlet is defined as a velocity inlet and the velocity is calculated based on the advance coefficient J, and a constant pressure that has the same value as the ambient pressure is set at the outlet. As for the far-field, a symmetry boundary condition is applied where the velocity gradient along the normal direction is zero. The surfaces of the propeller, rim and duct are considered as no-slip walls. To ensure a uniform and undisturbed inflow, the propeller is placed 4D downstream of the inlet. The outlet, on the other hand, is located 10D downstream to guarantee a fully developed wake flow. Moreover, the computational domain is composed of two zones, one static zone containing the fixed parts of the propeller and the other rotating zone containing the rotational parts of the propeller.

Table 5. Definition of boundary conditions for the computational domain.

Boundary	Velocity	Pressure
Inlet	Calculated by J	$\frac{\partial p}{\partial n} = 0$
Outlet	$\frac{\partial v}{\partial n} = 0$	Constant
Propeller, rim and duct	v=0	$\frac{\partial p}{\partial n} = 0$
Cylinder surface	$\frac{\partial v}{\partial n} = 0$	$\frac{\partial p}{\partial n} = 0$

The hydrodynamic coefficients are defined as

$$J = \frac{V_A}{nD}, \tag{8}$$

$$K_T = \frac{T}{\rho n^2 D^4}, \tag{9}$$

$$K_Q = \frac{Q}{\rho n^2 D^5}, \tag{10}$$

$$\eta = \frac{J}{2\pi} \frac{K_T}{K_Q}, \tag{11}$$

$$C_p = \frac{p - p_\infty}{\frac{1}{2}\rho V^2}, \tag{12}$$

$$C_f = \frac{\tau_w}{\frac{1}{2}\rho V^2}, \tag{13}$$

where V_A is the velocity given at the inlet, n is the propeller rotational speed, D the propeller diameter, J is the dimensionless advance ratio, K_T is the dimensionless total thrust coefficient, T is the total thrust, K_Q is the dimensionless torque coefficient, Q is the total torque, and η the hydrodynamic efficiency. It needs to be noted that the total thrust consists of a thrust contribution from the propeller T_P, rim T_R and duct T_D, and the total torque consists of a thrust contribution from the propeller Q_P and rim Q_R. C_p is the pressure coefficient, p is the local pressure, p_∞ is the pressure in the free-stream and V is the representative velocity of the propeller, which is equal to $\sqrt{V_A^2 + (0.7\pi n D)^2}$ and $\tau_w = \mu \frac{\partial u}{\partial y}\big|_{y=0}$ (u is the flow velocity along the blade surface, y is the normal distance).

The mesh distribution of the ducted propeller is illustrated in Figure 7. The trimmed mesh generator in Star-CCM+ was employed to generate unstructured cells around the propeller, with some refinement in the gap and wake regions. The estimation of discretization error for the ducted propeller is presented in Table 6. The total number of cells used for each case is provided, along with the refinement ratio calculated based on Equation (5). It can be observed that the results between different meshes are very close, particularly between the medium and fine meshes. The *GCI* values also indicate that the simulations are well converged, with a numerical uncertainty less than 2%. Moreover, by comparing the numerical results against experimental data, it is seen that the difference in propeller thrust is rather small, i.e., within 1.5%. For the propeller torque, the discrepancy is larger, but it is still within 3%. Considering the negligible variance between the medium and fine meshes, the medium mesh is considered to be fine enough to obtain accurate results regarding hydrodynamic characteristics of the studied propellers. Thus, the topology of the medium mesh is employed for the subsequent simulations.

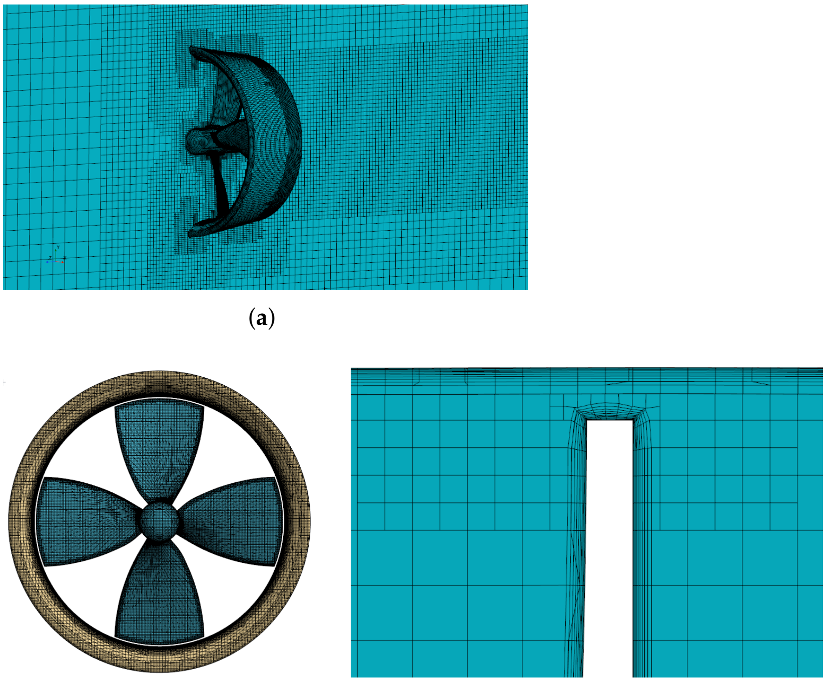
(**a**)

(**b**) (**c**)

Figure 7. Mesh distribution around the ducted propeller. (**a**) Overall mesh of the ducted propeller. (**b**) Surface mesh on the duct and propeller. (**c**) Mesh details near the blade tip clearance.

Table 6. Discretization error estimation for the ducted propeller.

Mesh Density	Total Cells	Refinement Ratio	$K_T/10K_Q$	*GCI*
Coarse	1,627,744	-	0.476/0.457	-
Medium	4,137,873	1.36	0.475/0.449	0.2%/2%
Fine	6,232,051	1.15	0.476/0.449	0.6%/≈0%
Experiment			0.468/0.437	

2.3.2. Open Water Performance Comparison

For the sake of completeness, the open water performance of the ducted propeller under a wide range of advance coefficients is provided in Figure 8. It can be observed that the correlations between numerical simulations and experimental measurements are fairly reasonable, especially for the propeller and duct thrust coefficients. The discrepancy in thrust coefficients between CFD and EFD is within 3% for all considered advance coefficients. As for the propeller torque coefficient, the CFD results are always lower than the experimental results. This can be attributed to the turbulence model used in the simulations, which is mainly empirically based and can hardly resolve the exact flow details in the boundary layer on the propeller surfaces. As such, the disagreement in efficiency is primarily caused by a torque difference.

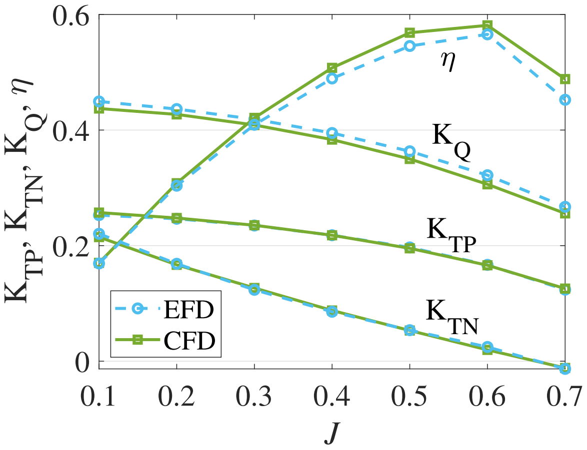

Figure 8. Open water performance of the ducted propeller.

The same meshing strategy for the ducted propeller is employed for the RDT. The basic parameters of the RDT are given in Table 7. The propeller is modified from a Ka propeller with a diameter of 0.25 m. In order to fit the peculiar structure of the RDT, the thickness distribution of the blade along the radial direction is reversed from the original one. As for the duct design, two duct forms are considered: one is directly adapted from the conventional 19A duct and the other one taken from Liu et al. [21] in order to take into account the accommodation of motor stator, as shown in Figure 9.

Table 7. Basic parameters of the RDT model used in this study.

Parameter	Symbol	Unit	Value
Number of blades	Z	-	4
Diameter of propeller	D_P	m	0.25
Area ratio of propeller	AR	-	0.72
Length of duct	L_D	m	0.1635
Length of rim	L_R	m	0.066
Height of rim	H	m	0.006
Rim gap width	W_G	m	0.002

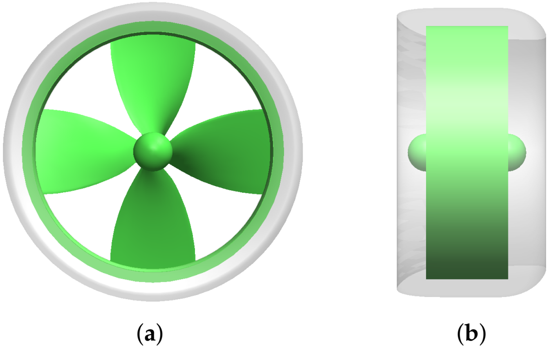
(**a**) (**b**)

Figure 9. The physical model of the rim-driven thruster. (**a**) Front view. (**b**) Side view.

Figure 10 presents the mesh distribution around the AFF-8 model with an RDT as propulsor. As can be seen in Figure 10a, there are some refinement zones in the computational domain, such as in the wakes of both the suboff and RDT, in order to better resolve the flow field and improve the prediction accuracy. Prism layers with a growth ratio of 1.2 are employed on the propeller and duct surfaces, and more importantly in the gap region of the RDT, as the gap flow has significant impacts on the performance of the RDT [12,34], as shown in Figure 10c.

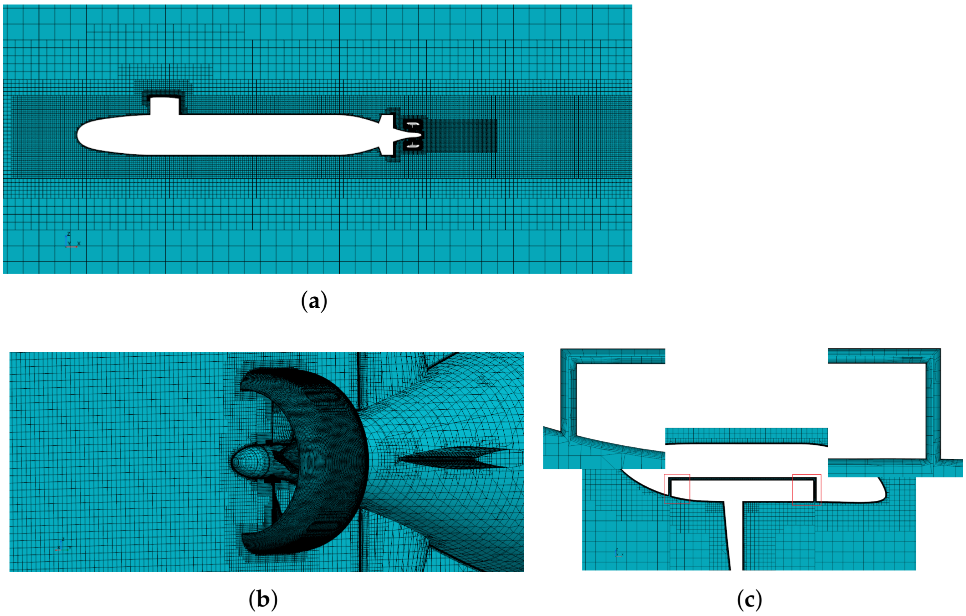
(**a**)

(**b**) (**c**)

Figure 10. Mesh distribution around the self-propulsion suboff AFF-8 model. (**a**) Overall mesh for the DARPA suboff AFF-8 with RDT. (**b**) Surface mesh at the stern of the suboff submarine. (**c**) Mesh details in the gap region.

3. Results and Discussion for the RDT

3.1. Self-Propulsion Characteristics

Currently, most research has assumed that RDTs work underwater as an isolated object. However, in practical cases, the hull of ships or underwater vehicles will pose significant influences on the propeller when moving through water, i.e., in the form of propeller–hull interactions. As a result, the effective flow velocity V_A to the propeller is no longer equal to the velocity of the incoming flow V_S (the advance velocity of the hull) as in the case of open water conditions. Therefore, the propeller thrust and torque are different. Moreover, the rotational movement of the propeller accelerates the flow at the stern of the hull and causes a pressure drop in this region, leading to an increase of the hull resistance compared to the case without propeller present. In order to quantify the self-propulsion characteristics, hydrodynamic coefficients recommended by ITTC [35] are introduced and briefly described below. The nominal wake field is the wake field of a ship or underwater vehicle at the propeller plane when the propeller is absent. The nominal wake coefficient w is used to reflect the degree to which the propeller is affected by the hull and is defined as

$$w = 1 - \frac{V_A}{V_S}, \tag{14}$$

where V_A represents the effective flow velocity to the propeller and V_S the advance velocity of the hull.

On the contrary, the total resistance of the hull is also influenced by the presence of the propeller. Due to the gain in hull resistance R, the propeller has to produce a higher thrust to overcome the additional resistance in order to keep the balance between forces. Since the additional resistance is caused by the propeller, it is often referred as thrust deduction, and the thrust deduction coefficient t is defined as

$$t = 1 - \frac{R}{T}, \tag{15}$$

where R is the total resistance of the hull without propeller, and T is the propeller thrust in self-propulsion conditions.

As aforementioned, the propeller thrust and torque behind a hull are distinct from those in open water due to the influence of the hull wake. Therefore, the thrust identity method is employed to relate the propeller efficiency in both cases. In open water conditions, the propeller's rotational rate is kept constant while the flow velocity is varied to obtain an identical thrust as for self-propulsion conditions. Assume that the thrust and torque of the propeller behind the hull are T and Q, respectively. Then the power P_D delivered to the propeller is defined as

$$P_D = 2\pi n Q, \tag{16}$$

where n is the rotational rate of the propeller. The propeller thrust power is calculated as

$$P_T = TV_A. \tag{17}$$

Then the ratio of P_T and P_D is considered as the efficiency of the propeller behind the hull, η_B, and is calculated as

$$\eta_B = \frac{TV_A}{2\pi n Q} = \frac{TV_A}{2\pi n Q_O}\frac{Q_O}{Q} = \eta_O \eta_R, \tag{18}$$

where Q_O is the propeller torque under open water conditions, η_O the open water efficiency and η_R the relative rotation efficiency. On the other hand, the hull efficiency η_H is the ratio of effective power P_E and propeller thrust power P_T and is calculated as

$$\eta_H = \frac{P_E}{P_T} = \frac{RV_S}{TV_A} = \frac{1-t}{1-w}. \tag{19}$$

Therefore, the propulsion efficiency η_D is calculated as

$$\eta_D = \eta_O \eta_R \eta_H. \tag{20}$$

Influence of Duct Profiles

In order to investigate the influence of propeller–hull interactions on the hydrodynamic performance of the RDT, the self-propulsion characteristics of the AFF-1 and AFF-8 models with an RDT under various flow velocities are explored using steady simulations with the MRF approach. Considering that in the non-uniform wake of an underwater vehicle the duct profile has a significant influence on the performance of the RDT by changing the attack angle of the propeller, RDTs with different duct profiles are also examined. One of them is modified from a conventional 19A duct as in the research of Liu and Vanierschot [12], Jiang et al. [34], Chen et al. [36], Lin et al. [37], Cai et al. [38], and the other from Liu et al. [21]. The 19A duct is commonly adopted in ducted propellers because it demonstrates excellent performance, particularly under heavy propeller loading conditions. The profiles and basic parameters of the two ducts are provided in Figure 11 and Table 8 to illustrate the difference. The thickness of the optimized duct is selected according to the thickness of the 19A duct at the middle position.

Table 8. Basic parameters of the RDT ducts.

Parameter	Symbol	Unit	Value
Length of duct	L_D	m	0.1635
Inner radius	D_i	m	0.25
Outer radius	D_o	m	0.3

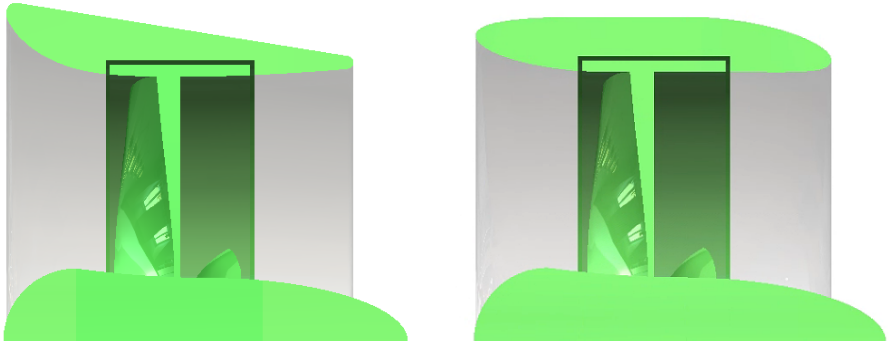
(**a**) (**b**)

Figure 11. The scheme of duct profiles used in this study. (**a**) RDT with 19A duct form (*RDT-19A*). (**b**) RDT with OPT duct form (*RDT-OPT*).

The self-propulsion characteristics of the AFF-1 with two RDT configurations are provided in Figure 12a. For each advance speed, the self-propulsion point was defined by searching for the rotational speed of the propeller when the total thrust produced by the RDT overcomes the total resistance of the suboff model. The advance coefficient J is obtained from the thrust identity method. It can be seen that the advance coefficient increases gradually with an increase of advance speed of the submarine. However, the increase in J as a function of advance speed is not as significant, since the propeller's rotational speed also increases to produce sufficient thrust to overcome the greater hull resistance. It is also noted that the advance coefficient of the *RDT-OPT* is always higher than that of *RDT-19A*. Moreover, the influence of the submarine hull on *RDT-19A* is more pronounced, as indicated by the wake fraction coefficient w. However, with an increase of advance speed, the effect of the submarine wake is gradually reduced. As for the thrust deduction coefficient, the RDT shows more intense interactions with the submarine hull, resulting in a higher resistance.

The hull efficiency represents the relationship between wake fraction coefficient and thrust deduction coefficient. As mentioned above, the wake fraction coefficient mainly reflects the influence of the vessel hull on the propeller. The thrust deduction coefficient, on the other hand, is responsible for the extra resistance production on the hull caused by the suction action of the propeller. When the wake fraction coefficient is larger than the thrust deduction coefficient, the hull efficiency will be larger than unity, which is the case for both *RDT-OPT* and *RDT-19A*. It is also observed that the hull efficiency of *RDT-19A* is higher than the one of *RDT-OPT*. When the propeller works behind the hull, the actual velocity of the flow to the propeller is no longer constant or perpendicular to the propeller disk area. Therefore, the torque required for the propeller to produce an identical thrust becomes different. The relative rotation efficiency of *RDT-OPT* and *RDT-19A* is very close to one, with the former less than one and the latter larger than one. Even though there is a significant discrepancy in the open water efficiency η_O between *RDT-OPT* and *RDT-19A*, the difference in propulsion efficiency η_D is much less distinct, which suggests that due to the complex relationship between these parameters, considering only one or two parameters when evaluating the performance of a propeller may lead to failure to make an accurate estimation. Nevertheless, when behind the hull form of the AFF-1, the *RDT-OPT* has exhibited better performance in improving the propulsion efficiency compared to *RDT-19A* for all considered advance speeds. Compared to AFF-1, there is a small difference in the self-propulsion characteristics of AFF-8, as shown in Figure 12b. The advance coefficient, wake fraction coefficient and thrust deduction coefficient of RDT still follow the same pattern as for AFF-1, but the discrepancy from *RDT-19A* becomes smaller. It is noteworthy that the hull efficiency decreases for both RDTs. Consequently, even though the open water efficiency improves as compared to the AFF-1 case, the propulsion efficiency declines at the corresponding advance speed. Again, the *RDT-OPT* demonstrates improved propulsion efficiency compared to *RDT-19A* for most advance speeds.

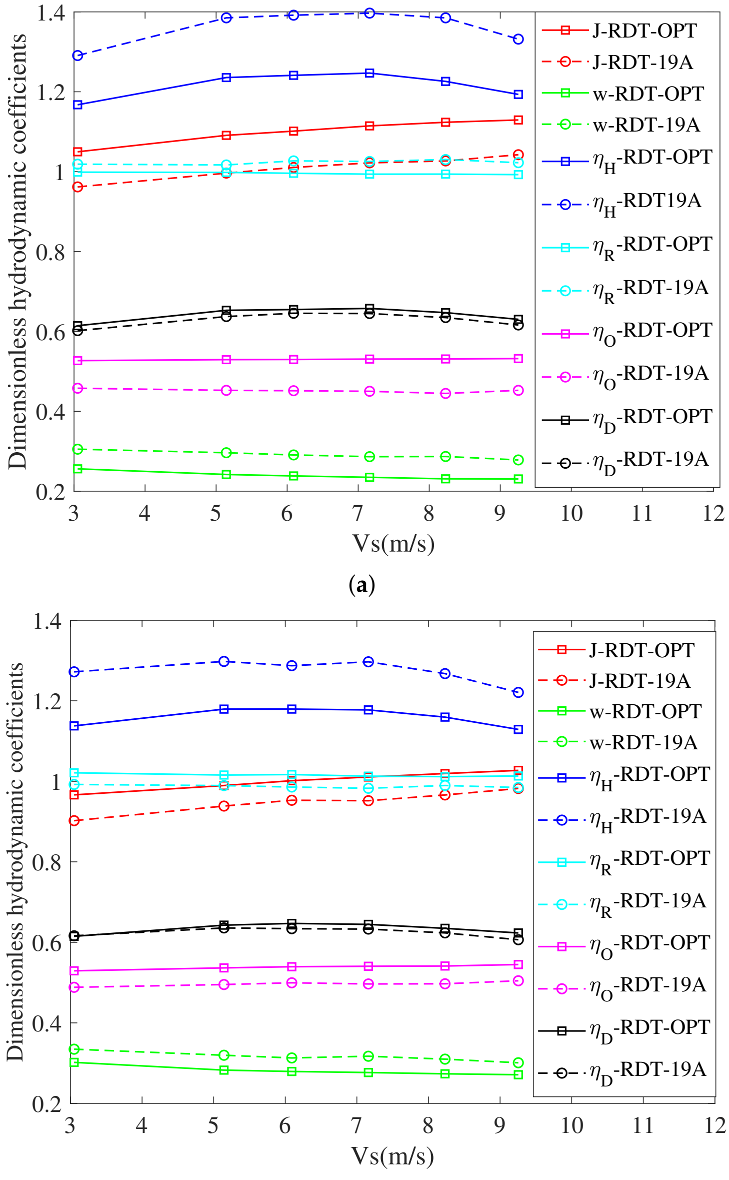

(**a**)

(**b**)

Figure 12. Self-propulsion characteristics of AFF-1 and AFF-8 with RDTs. (**a**) AFF-1+RDTs. (**b**) AFF-8+RDTs.

3.2. Flow Field Analysis

To better illustrate the interaction between the RDT and submarine hull, a comparison of pressure coefficient distribution over the submarine surfaces with and without RDTs is presented in Figure 13. As can be seen, the influence of the propeller on the submarine is mainly focused on the stern region where a clear pressure drop is observed when the propeller is present (the discontinuity in the plot is where the propeller is located, as indicated by the black circle). This shows that the rotational movement of the propeller accelerates the flow nearby, and consequently the local pressure is reduced. A close-up of the pressure coefficient distribution where the pressure starts to decline is also provided in each plot. As expected, the pressure drop caused by the *RDT-OPT* is more substantial than that of *RDT-19A*, resulting in a higher resistance of the submarine hull.

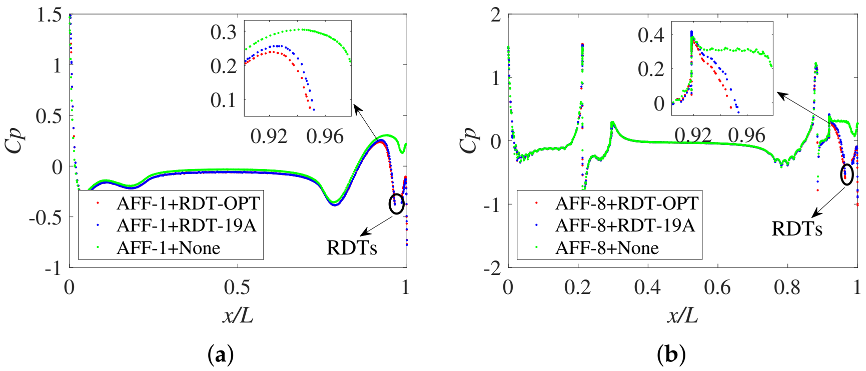

(**a**) (**b**)

Figure 13. Influence of propeller motion on the pressure distribution on the submarine surfaces. (**a**) AFF-1. (**b**) AFF-8.

The velocity distributions at a cross-sectional plane just upstream of the propeller for the AFF-8 with two RDT configurations are compared in Figure 14 to demonstrate the influence of the propeller–hull interactions on the flow field. Again the presented velocity is the streamwise velocity, which has been non-dimensionalized by the freestream velocity. It can be observed that the velocity vectors are pointed to the hub center, which is caused by the suction effect of the propeller. The velocity profiles around the propeller exhibit a similar pattern, with a velocity magnitude changing gradually along the radial direction. The effects of submarine rudders and stern are clearly visible, with a low axial speed wake caused by the necklace vortices generated on these appendages, as reported by Chase et al. [32]. The reduction in velocity can result in a higher propeller loading, and thus more intense pressure fluctuations. It is noted that the the low velocity region of the *RDT-19A* configuration is obviously larger than the one of the *RDT-OPT* configuration, and consequently the effective advance coefficient is lower, which is consistent with the results shown in Figure 12b.

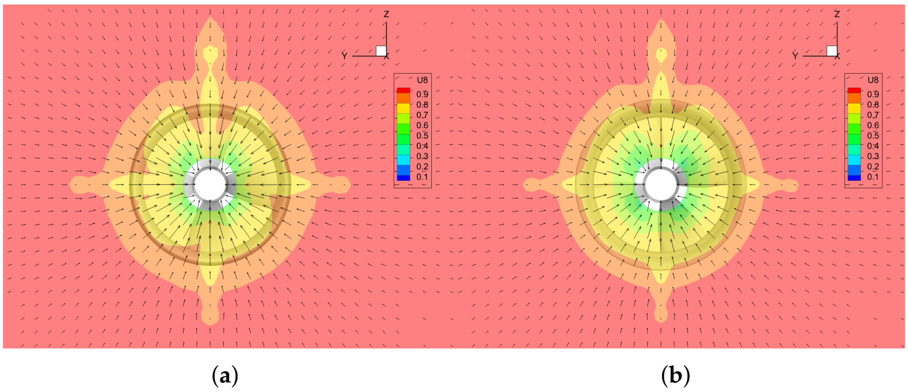

(**a**) (**b**)

Figure 14. The comparison of velocity distribution upstream the RDTs behind the AFF-8 submarine. (**a**) AFF-8+*RDT-OPT*. (**b**) AFF-8+*RDT-19A*.

Due to the rotational movement of the propeller, the flow field often changes in a periodic manner with a frequency corresponding to the blade passing frequency (BPF), which is 36 1/s in the considered case. In order to quantify the pressure fluctuations caused by the interactions between RDT and submarine hull, two probing points are located 0.5D upstream the propeller and two points 0.5D downstream to monitor the pressure changes, as illustrated in Figure 15. Then unsteady simulations with the sliding mesh approach are carried out to study the pressure fluctuations in the flow field near the RDT. The pressure fluctuations normalized by $\frac{1}{2}\rho n^2 D^2$ after five propeller rotational cycles are presented in Figure 16. It can be seen that the pressure coefficients change periodically with almost constant amplitude for both the *RDT-OPT* and *RDT-19A* configurations. However, the amplitude of pressure fluctuations at different positions is obviously distinct, with point 1 and point 3 exhibiting higher orders than point 2 and point 4. This may suggest that the strength of the vortex shed from the stern decreases along the spanwise direction, and the interactions of vortices at the outer radius of the propeller are more intense, resulting in higher pressure fluctuations. Moreover, a Fast Fourier Transform (FFT) is employed to change the data in the time domain into the frequency domain for further analysis. As can be seen from Figure 17a–d, the amplitude of the pressure fluctuations at the BPF has the highest peak compared to its harmonics, and the *RDT-OPT* configuration always shows higher values than that of the *RDT-19A* configuration, indicating a more intense interaction with the submarine hull.

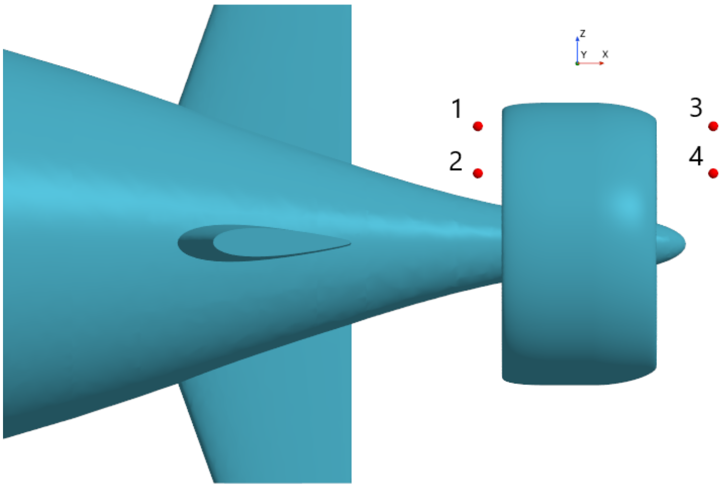

Figure 15. The position of probing points used for the analysis of fluctuating pressure.

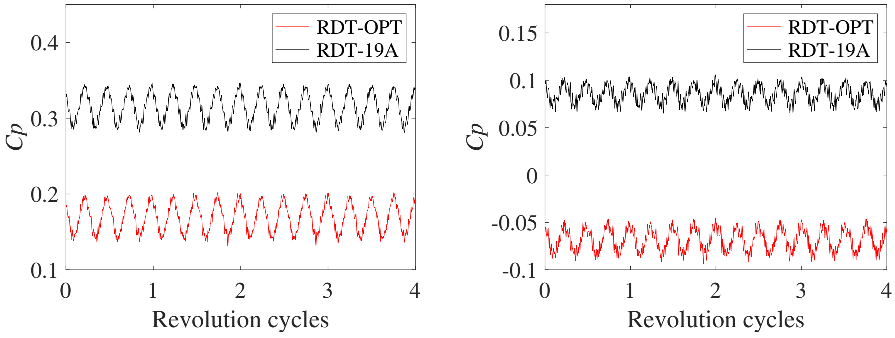

(**a**) (**b**)

Figure 16. *Cont.*

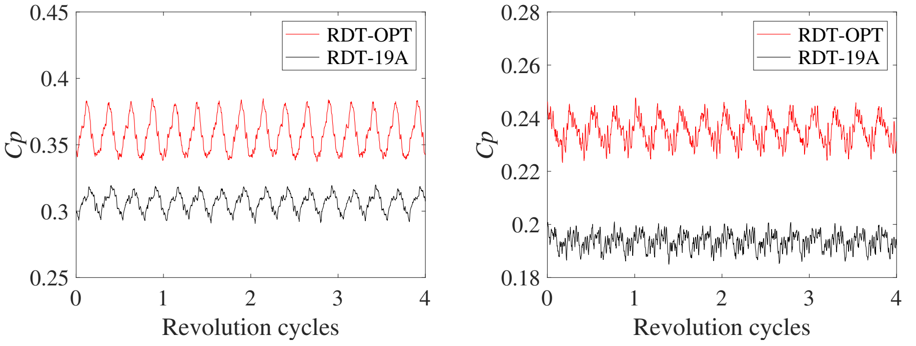

(**c**) (**d**)

Figure 16. Comparison of pressure coefficient fluctuations at the probing points near the RDTs. (**a**) Probing point 1. (**b**) Probing point 2. (**c**) Probing point 3. (**d**) Probing point 4.

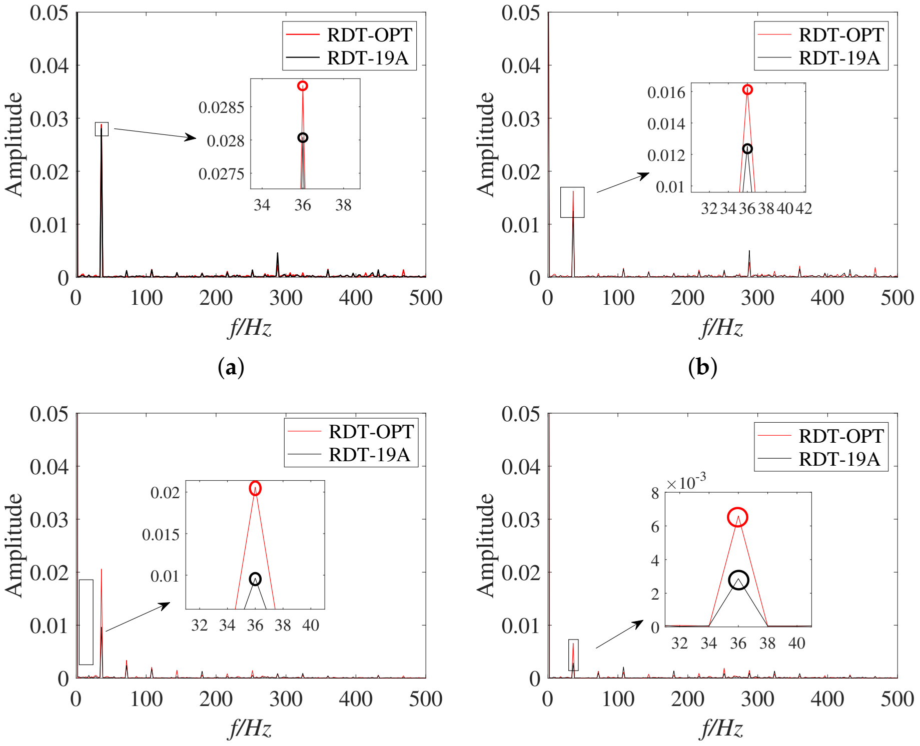

(**a**) (**b**)

(**c**) (**d**)

Figure 17. Comparison of amplitude of pressure coefficient fluctuations at the probing points near the RDTs. (**a**) Probing point 1. (**b**) Probing point 2. (**c**) Probing point 3. (**d**) Probing point 4.

4. Conclusions

The present work investigates the influence of propeller–hull interactions on the hydrodynamic performance of RDTs. RDTs with different duct profiles are assumed to operate in the wake of the DARPA suboff submarine models AFF-1 and AFF-8. A grid sensitivity analysis and validation study are carried out to ensure good numerical accuracy. Afterwards, the self-propulsion characteristics of the suboff models with two RDT configurations under a wide range of advance speeds are considered to perform a reasonable comparison. The unsteady flow fields are then presented and analyzed to explain the differences in flow fields. Based on the results, some findings and conclusions are summarized below.

- Due to the presence of the submarine hull, the RDTs show distinct hydrodynamic characteristics compared to the cases in open water conditions. Moreover, the shape of the submarine hull can have an obvious influence on the performance of the RDTs.
- The effective advance coefficient of the RDTs increases with the advance speed of the submarine in a non-linear manner. The duct profile also has a significant effect on the flow behavior upstream of the propeller, resulting in different equivalent advance coefficients under the same submarine advance speed.
- The profile of the RDT duct has a significant influence on the hydrodynamic characteristics of the RDT under self-propulsion conditions, as well as the pressure fluctuations in the flow fields near the RDTs.
- The wake of the submarine hull is no longer uniform as in the case of open water conditions, and the vortex generated on the sterns of the AFF-8 causes more intense interactions with the RDTs.
- The pressure fluctuations display a higher amplitude at regions near the propeller tip compared to regions near the hub, indicating the pattern of vortex distribution in the stern wake.
- The fundamental frequency of the pressure fluctuations corresponds to the blade passing frequency, and its higher harmonics are almost negligible in terms of amplitude.

Given the complex interactions between the submarine hull and RDTs, considering only the open-water performance of RDTs may not be sufficient for optimal designs aimed at improving efficiency. The results presented here can provide some insight into the evaluation of the comprehensive performance of RDTs, which may help RDT designers make better choices during the design process.

Author Contributions: Conceptualization, B.L., M.V. and W.O.; methodology, B.L.; software, W.O.; validation, B.L. and W.O.; formal analysis, B.L.; investigation, B.L.; resources, B.L. and X.Y.; data curation, B.L.; writing—original draft preparation, B.L.; writing—review and editing, M.V. and W.O.; visualization, B.L.; supervision, X.Y., M.V. and W.O.; project administration, W.O.; funding acquisition, X.Y. All authors have read and agreed to the published version of the manuscript.

Funding: This research is financially supported by the National Key R&D Program of China (No. 2022YFB4300802) and the Fundamental Research Funds for the Central Universities (WUT: 2023IVA084).

Data Availability Statement: Data will be available upon request.

Conflicts of Interest: The authors declare no conflict of interest.

Abbreviations

CFD	Computational Fluid Dynamics
DARPA	Defense Advanced Research Projects Agency
EFD	Experimental Fluid Dynamics
RANS	Reynolds-Averaged Navier Stokes
DES	Detached Eddy Simulation
RDT	Rim-driven Thruster
UV	Underwater Vehicle
SST	Shear Stress Transport
SIMPLE	Semi-Implicit Method for Pressure Linked Equation
MRF	Moving Reference Frame
RPM	Revolutions Per Minute
SM	Sliding Mesh

References

1. Yan, X.; Liang, X.; Ouyang, W.; Liu, Z.; Liu, B.; Lan, J. A review of progress and applications of ship shaft-less rim-driven thrusters. *Ocean Eng.* **2017**, *144*, 142–156. [CrossRef]
2. Li, P.; Yao, H.; Wang, C.; Weng, K. Improved efficiency with concave cavities on S3 surface of a rim-driven thruster. *Phys. Fluids* **2023**, *35*, 107102. [CrossRef]

3. Tuohy, P.; Smith, A.; Husband, M.; Hopewell, P. Rim-drive marine thruster using a multiple-can induction motor. *IET Electr. Power Appl.* **2013**, *7*, 557–565. [CrossRef]
4. Richardson, K.; Pollock, C.; Flower, J. Design of a switched reluctance sector motor for an integrated motor/propeller unit. In Proceedings of the Electrical Machines and Drives, Durham, UK, 11–13 September 1995; pp. 271–275.
5. Sharkh, S.; Lai, S. Slotless PM brushless motor with helical edge-wound laminations. *IEEE Trans. Energy Convers.* **2009**, *24*, 594–598. [CrossRef]
6. Hassannia, A.; Darabi, A. Design and Performance Analysis of Superconducting Rim-Driven Synchronous Motors for Marine Propulsion. *IEEE Trans. Appl. Supercond.* **2013**, *24*, 40–46. [CrossRef]
7. Dubas, A.; Bressloff, N.; Sharkh, S. Numerical modelling of rotor–stator interaction in rim driven thrusters. *Ocean Eng.* **2015**, *106*, 281–288. [CrossRef]
8. Liu, B.; Vanierschot, M.; Buysschaert, F. Effects of transition turbulence modeling on the hydrodynamic performance prediction of a rim-driven thruster under different duct designs. *Ocean Eng.* **2022**, *256*, 111142. [CrossRef]
9. Liu, B.; Vanierschot, M.; Buysschaert, F. Comparison Study of the $k - k_L - \omega$ and $\gamma - Re_\theta$ Transition Model in the Open-Water Performance Prediction of a Rim-Driven Thruster. *Int. J. Turbomach. Propuls. Power* **2024**, *9*, 2. [CrossRef]
10. Grlj, C.G.; Degiuli, N.; Farkas, A.; Martić, I. Numerical Study of Scale Effects on Open Water Propeller Performance. *J. Mar. Sci. Eng.* **2022**, *10*, 1132. [CrossRef]
11. Li, P.; Sun, C.; Yao, H.; Wang, Z.; Wang, C.; Weng, K. The effects of domain division types on the performance prediction of a rim-driven thruster. *Ocean Eng.* **2023**, *287*, 115809. [CrossRef]
12. Liu, B.; Vanierschot, M. Numerical Study of the Hydrodynamic Characteristics Comparison between a Ducted Propeller and a Rim-Driven Thruster. *Appl. Sci.* **2021**, *11*, 4919. [CrossRef]
13. Song, B.; Wang, Y.; Tian, W. Open water performance comparison between hub-type and hubless rim driven thrusters based on CFD method. *Ocean Eng.* **2015**, *103*, 55–63. [CrossRef]
14. Liu, B.; Vanierschot, M.; Buysschaert, F. Numerical study of scale effects on the open water performance of a rim-driven thruster. *Appl. Ocean Res.* **2023**, *138*, 103667. [CrossRef]
15. Liu, B.; Dai, M.; Liang, X. Influence of bearings on the open water performance of a rim-driven thruster. *Phys. Fluids* **2023**, *138*, 085139. [CrossRef]
16. Liu, B.; Yan, X.; Ouyang, W.; Vanierschot, M. Comparison study of the vortical structures in the wake of a rim-driven thruster and a ducted propeller in bollard conditions. *Ocean Eng.* **2024**, *306*, 118064. [CrossRef]
17. Gaggero, S. A Study on the Wake Evolution of a Set of RIM-Driven Thrusters. *J. Mar. Sci. Eng.* **2023**, *11*, 1659. [CrossRef]
18. Song, K.; Kang, Y. A numerical performance analysis of a rim-driven turbine in real flow conditions. *J. Mar. Sci. Eng.* **2022**, *10*, 1185. [CrossRef]
19. Gaggero, S. Numerical design of a Rim-driven thruster using a RANS-based optimization approach. *Appl. Ocean Res.* **2020**, *94*, 101941. [CrossRef]
20. Zhai, S.; Jin, S.; Chen, J.; Liu, Z.; Song, X. CFD-based multi-objective optimization of the duct for a rim-driven thruster. *Ocean Eng.* **2022**, *264*, 112467. [CrossRef]
21. Liu, B.; Vanierschot, M.; Buysschaert, F. Optimization design of the duct of a rim-driven thruster using the adjoint approach. *Ocean Eng.* **2023**, *278*, 114293. [CrossRef]
22. Nie, Y.; Ouyang, W.; Zhang, Z.; Li, G.; Zheng, R. Multi-Parameter Optimization Analysis of Hydrodynamic Performance for Rim-Driven Thruster. *Energies* **2023**, *16*, 891. [CrossRef]
23. Woeste, J.; O'Reilly, C.; Gouveia, R.; Young, Y. Propeller–hull interactions and added power in head seas. *Ocean Eng.* **2022**, *247*, 110630. [CrossRef]
24. Guo, H.; Zou, Z.; Liu, Y.; Wang, F. Investigation on hull-propeller-rudder interaction by RANS simulation of captive model tests for a twin-screw ship. *Ocean Eng.* **2018**, *162*, 259–273. [CrossRef]
25. Dogrul, A. Numerical prediction of scale effects on the propulsion performance of Joubert BB2 submarine. *Brodogradnja* **2022**, *73*, 17–42.
26. Li, S.; Xiao, C.; Cao, Z. Numerical analysis of wake flow and hydrodynamics for a submarine based on STAR-CCM+. *Chin. J. Ship Res.* **2018**, *13*, 29–35.
27. Posa, A.; Balaras, E. A numerical investigation of the wake of an axisymmetric body with appendages. *J. Fluid Mech.* **2016**, *792*, 470–498. [CrossRef]
28. Menter, F. Two-equation eddy-viscosity turbulence models for engineering applications. *AIAA J.* **1994**, *32*, 1598–1605. [CrossRef]
29. Huang, T.; Liu, H. Measurements of Flows over an Axisymmetric Body with Various Appendages in a Wind Tunnel: The Darpa Suboff Experimental Program. In Proceedings of the 19th Symposium on Naval Hydrodynamics, Washington, DC, USA, 24–28 August 1994; pp. 312–346.
30. Roache, P.J. Quantification of uncertainty in computational fluid dynamics. *Annu. Rev. Fluid Mech.* **1997**, *29*, 123–160. [CrossRef]
31. Liu, H.; Huang, T. *Summary of DARPA Suboff Experimental Program Data*; Carderock Division, Naval Surface Warfare Center: West Bethesda, MD, USA, 1998.
32. Chase, N.; Michael, T.; Carrica, P. Overset simulation of a submarine and propeller in towed, self-propelled and maneuvering conditions. *Int. Shipbuild. Prog.* **2013**, *60*, 171–205.
33. Oosterveld, M. Wake Adapted Ducted Propellers. Ph.D. Thesis, TU Delft, Delft, The Netherlands, 1970.

34. Jiang, H.; Ouyang, W.; Sheng, C.; Lan, J.; Bucknall, R. Numerical investigation on hydrodynamic performance of a novel shaftless rim-driven counter-rotating thruster considering gap fluid. *Appl. Ocean Res.* **2022**, *118*, 102967. [CrossRef]
35. ITTC. Report of Performance Committee. In Proceedings of the 15th ITTC, The Hague, The Netherlands, 3–10 September 1978.
36. Chen, C.; Chen, X.; Zhou, Z.; Zhang, C.; Chen, J.; Zheng, T. The effect of tip rake distribution on the hydrodynamic performance of shaftless rim-driven contra-rotating thruster. *Ocean Eng.* **2023**, *285*, 115454. [CrossRef]
37. Lin, J.; Yao, H.; Wang, C.; Sun, Y.; Yang, C. Hydrodynamic performance of a rim-driven thruster improved with gap geometry adjustment. *Eng. Appl. Comput. Fluid Mech.* **2023**, *17*, 2183902. [CrossRef]
38. Cai, M.; Yang, C.; Wu, S.; Zhu, Y.; Xie, Y. Hydrodynamic analysis of a rim-driven thruster based on RANS method. In Proceedings of the OCEANS 2015-MTS/IEEE, Washington, DC, USA, 19–22 October 2015; pp. 1–5.